Hydrophobic molecular assembly at the gas-liquid-solid interface drives highly selective CO$_2$ electromethanation

Morgan McKee[1], Maximilian Kutter[2,3], Dieter Lentz[4], Moritz F. Kühnel[2,5]* and Nikolay Kornienko[1]*

[1]Department of Chemistry, Université de Montréal, 1375 Ave. Thérèse-Lavoie-Roux, Montréal, QC H2V 0B3, Canada

[2]Department of Chemistry, Swansea University, Singleton Park, Swansea SA2 8PP, Wales, UK

[3]Electrochemical Process Engineering, Universität Bayreuth, Universitätsstraße 30, 95447 Bayreuth, Germany

[4]Freie Universität Berlin, Institut für Chemie und Biochemie – Anorganische Chemie, Fabeckstraße 34-36, 14195 Berlin, Germany

[5]Fraunhofer Institute for Wind Energy Systems IWES, Am Haupttor BC 4310, 06237 Leuna, Germany

*Correspondence to: m.f.kuehnel@swansea.ac.uk and nikolay.kornienko@umontreal.ca

Abstract

The modularity of molecular catalysts enables the tuning of both active site and peripheral units to maximize functionality, thus rendering them as ideal model systems to explore fundamental concepts in catalysis. Hydrophobicity is often regarded as an undesirable aspect that hinders their dissolution in aqueous electrolytes. In contrast, we modified established Co terpyridine catalysts with hydrophobic perfluorinated alkyl side chains and took advantage of their hydrophobic character by utilizing them not as dissolved species in an aqueous electrolyte but at the gas-liquid-solid interfaces on a gas diffusion electrode (GDE) applied towards the electrochemical reduction of CO$_2$. We found that the self-assembly of these perfluorinated units on the GDE surface results in a catalytic system selective for CH$_4$ production, whereas every other Co terpyridine catalyst reported before was only selective for CO or formate. An array of mechanistic and *operando* spectroscopic investigations suggests a mechanism in which the pyridine units function as proton shuttles that deliver protons to the dynamic hydrophobic pocket in which CO$_2$ reduction takes place. Finally, optimizing the system by integrating fluorinated carbon nanotubes as a hydrophobic conductive scaffold leads to a Faradaic efficiency for CH$_4$ production above 80% at rates above 10 mA cm^{-2}, thus far unprecedented for a molecular electrocatalytic system.

Introduction

Electrochemical carbon dioxide reduction (CO_2R) has attracted a wide amount of attention as a potential means to reduce reliance on fossil fuels by converting CO_2 into fuels and societally important chemicals.[1,2] In particular, this technology has the potential to contribute to a closed carbon cycle when powered by low-carbon renewable energy sources.[3,4] Amongst key challenges in advancing CO_2R systems towards practical use is the development of non-precious metal catalysts that can selectively reduce CO_2 into a single desired fuel and integrating them into a functional device.[5,6]

Molecular catalysts have long been studied as model systems for extracting important structure-activity relationships in CO_2R because binding site, functional ligands and reaction environment can all be precisely defined.[7,8] This offers particular advantages over heterogeneous catalysts which often have a diversity of possible active sites in generating fundamental insights that can later be translated to functional systems. To this end, most efforts in molecular CO_2R have been directed in either using the catalysts in homogeneous form, dissolved in an electrolyte, or heterogenized onto an electrode surface.[9,10] In aqueous electrolytes which are practical for CO_2R, excessive hydrophobicity often precluded certain catalysts from being applied for CO_2R as this prevented their dissolution for homogeneous applications or their capacity to effectively bind dissolved CO_2 and extract protons from water when they were heterogenized.

In contrast, hydrophobicity is advantageous for catalysts applied in gas diffusion electrodes, which feed CO_2 to the catalyst directly from the gas phase and the reaction largely occurs at a gas-liquid-solid interphase.[11] In this context, rationally incorporated hydrophobic elements have greatly boosted the performance of heterogeneous catalysts in GDE-based reactors.[12,13] However, these efforts to date have only been limited to heterogeneous catalysts. Molecular CO_2R catalysts have indeed been integrated with gas-fed flow cells and initial results have demonstrated that phthalocyanines/porphyrins,[14-17] Co quaterpyridine[18] and Ni cyclam[19] catalysts can also function in this geometry. However, most of these molecular systems have been metal complexes that possess an extended π-conjugated system that facilitates their ease of adsorption onto the carbon surfaces in a GDE. This presents a design constraint, though this can also be circumvented by using hydrophobic self-assembly to immobilize the catalysts on the GDE surface as an alternative route.

In this work, we demonstrate for the first time the deliberate integration of hydrophobicity into a molecular CO_2R catalyst operating at the gas-liquid-solid interface within a gas-diffusion electrode (Fig. 1a). Our system consists of Co terpyridine catalysts with perfluorinated alkyl chains (Co Terpy-R_F) that render the system hydrophobic due to the perfluoro-perfluoro interactions between the perfluorinated alkyl chains (Fig. 1b). To our surprise, the Co Terpy-R_F system was found to be selective for methane production, a stark contrast to other Co-pyridine catalysts that primarily produced CO or formate.[18,20-24]

A gamut of mechanistic investigations provided evidence that the catalysts operated within a hydrophobic catalytic pocket through which protons were shuttled via a pyridine ligand centered conduit. This unique environment altered the selectivity from CO to CH_4, with an optimized system featuring Faradaic efficiency (FE) above 80% at 10 mA cm^{-2}, a first for molecular CO_2R systems.
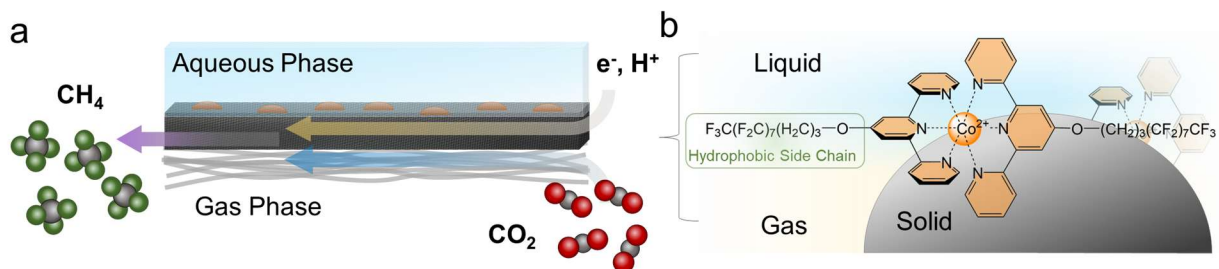
Figure 1. A simplified illustration of the gas-fed CO_2R reactor geometry used in this work (a) and structure of the molecular Co Terpy-R_F catalyst operating at the gas-liquid-solid interface (b).

Results and Discussion

The target hydrophobic electrocatalyst based on the well-known Co terpyridine catalyst motif[20,23,24] was synthesized by introduction of a perfluoroalkyl chain to the terpyridine ligand backbone *via* an ether linkage in the 4'-position (see Figs. S1-S4 for characterization).[25] A spacer of three ethylene groups between the terpyridine moiety and the fluorinated chain was chosen to avoid electronic effects on the catalyst, which have been previously found to affect the product selectivity in CO_2 reduction electrocatalysis.[24] The fluorinated bis(terpyridine) complex Co Terpy-R_F was self-assembled from 4'-((4,4,5,5,6,6,7,7,8,8,9,9,9-tridecafluorononyl)oxy)-2,2':6',2"-terpyridine (Terpy-R_F) and a cobalt(II) salt (Fig. 2a) in a 2:1 ratio; successful assembly of the homoleptic Co complex was corroborated by UV-Vis spectroscopy (Fig. S5) showing two absorption maxima at $\lambda = 452$ and 505 nm as well as by high-resolution mass spectrometry (Fig. S6).

Single-crystal structure determination further proved the identity of Co Terpy-R_F and illustrated the key role of hydrophobic interactions in its aggregation in the solid state (Fig. 2b, c, Table S1). The complex prefers to stack in a manner that maximizes the perfluoro-perfluoro interactions on its side chains through the formation of fluorinated domains, i.e. hydrophobic pockets.[26] At a macroscopic level, this is similarly manifested in a spontaneous crystallization into ordered ribbons that were on the order of several microns thick and tens of microns in length upon drying a solution of the complex on a solid substrate (Fig. 2d). The hydrophobicity of the Co Terpy-R_F film was estimated through contact angle measurements, which yielded a value of 100.7°, corresponding to an overall hydrophobic character (Fig. S7).

The strength of fluorous attractions exhibited by the fluoroalkyl chains was further demonstrated by using the fluorous tag on Co Terpy-R_F to attach it to a matching fluorous surface. To this end, indium tin oxide (ITO) was first modified with a fluoroalkyl phosphonic acid and subsequently incubated with a Co Terpy-R_F solution. After thorough washing, X-ray photoelectron spectroscopy (XPS) of the modified ITO showed signals in the Co 2p, F 1s and N 1s regions similar to those of the pure complex, confirming the Co Terpy-R_F was intact on the surface and strongly adheres to other fluorinated species (Fig. S8).
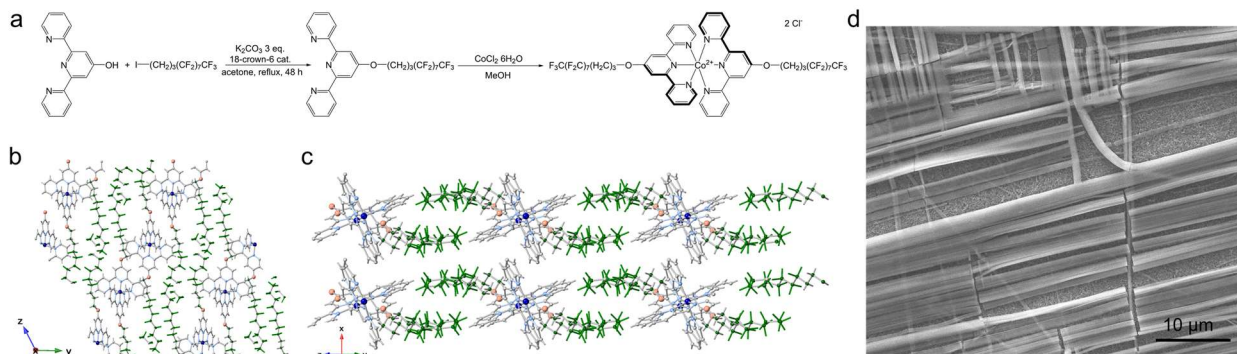
Figure 2. Reaction scheme for the synthesis of Co Terpy-O-R_F (a), crystal structure of Co Terpy-R_F with the perfluoro side chains depicted in green (b, c) and SEM image of the catalyst deposited on a carbon cloth electrode (d).

Electrochemical studies

We next investigated the capacity of Co Terpy-R_F to function as a CO_2R electrocatalyst in an acetonitrile solvent with tetrabutylammonium hexafluorophosphate supporting electrolyte. Under N_2, Co Terpy-R_F exhibited redox waves at 0.1 V and at –1.2 V vs. Fc^+/Fc (Fig. 3a and S9). From previous studies on analogous complexes, we assign the two waves to a Co(III/II) and a Co(II/I) redox couple, respectively.[24,27] Upon adding CO_2 to the system, we observed an irreversible catalytic current more negative than the Co(II/I) wave, indicating that Co Terpy-R_F in the Co(I) state is active towards CO_2R. After potentiostatic electrolysis, we measured CO as the primary product (see Fig. S10-12 for product analysis), albeit produced with only a modest 8.4% FE.

The same complex was dropcast onto a carbon cloth GDE and applied in a simplified flow cell as a heterogenized CO_2R catalyst using a $KHCO_3$ electrolyte (Fig. S13-14). The same Co(III/II) and Co(II/I) waves were observed at 0.8 and –0.2 V vs. RHE, alongside a catalytic current more negative than –0.2 V when CO_2 was flown through the cell (Fig. 3b). Electrochemical impedance spectroscopy (EIS) testing indicated that there were two main points of resistance, one attributed to electron transfer through the catalyst film, and another from the catalysis at the active sites (Fig. S15).[28] Resistance in charge transfer in the Co Terpy-R_F film is also evident in the increasingly large Co(II/III) peak separation as CV scan rates are increased (Fig. S16).

Under these conditions however, we observed CH_4 as the dominant product. Its production increased until –0.99 V vs. RHE, after which point the excessively negative potentials resulted in catalyst degradation (Fig. 3c). Quantifying the selectivity (FE) for all products observed, we noted that CH_4 production accounts for up to 60% of the total electron flow through the cathode at –0.79 V vs. RHE (Fig. 3d). Finally, we measured the stability of the system through an extended electrolysis at –0.79 V vs. RHE and recorded an overall FE for CH_4 of 71%. Based on the quantity of redox-active Co Terpy-R_F on the electrode, the turnover number for CH_4 production (TON_{CH4}) was >18,000. After this measurement, the electrode still exhibited the same spectroscopic signature

as prior to electrolysis and a similar visual appearance, pointing to a high stability of Co Terpy-R_F under these parameters (Fig. S17).
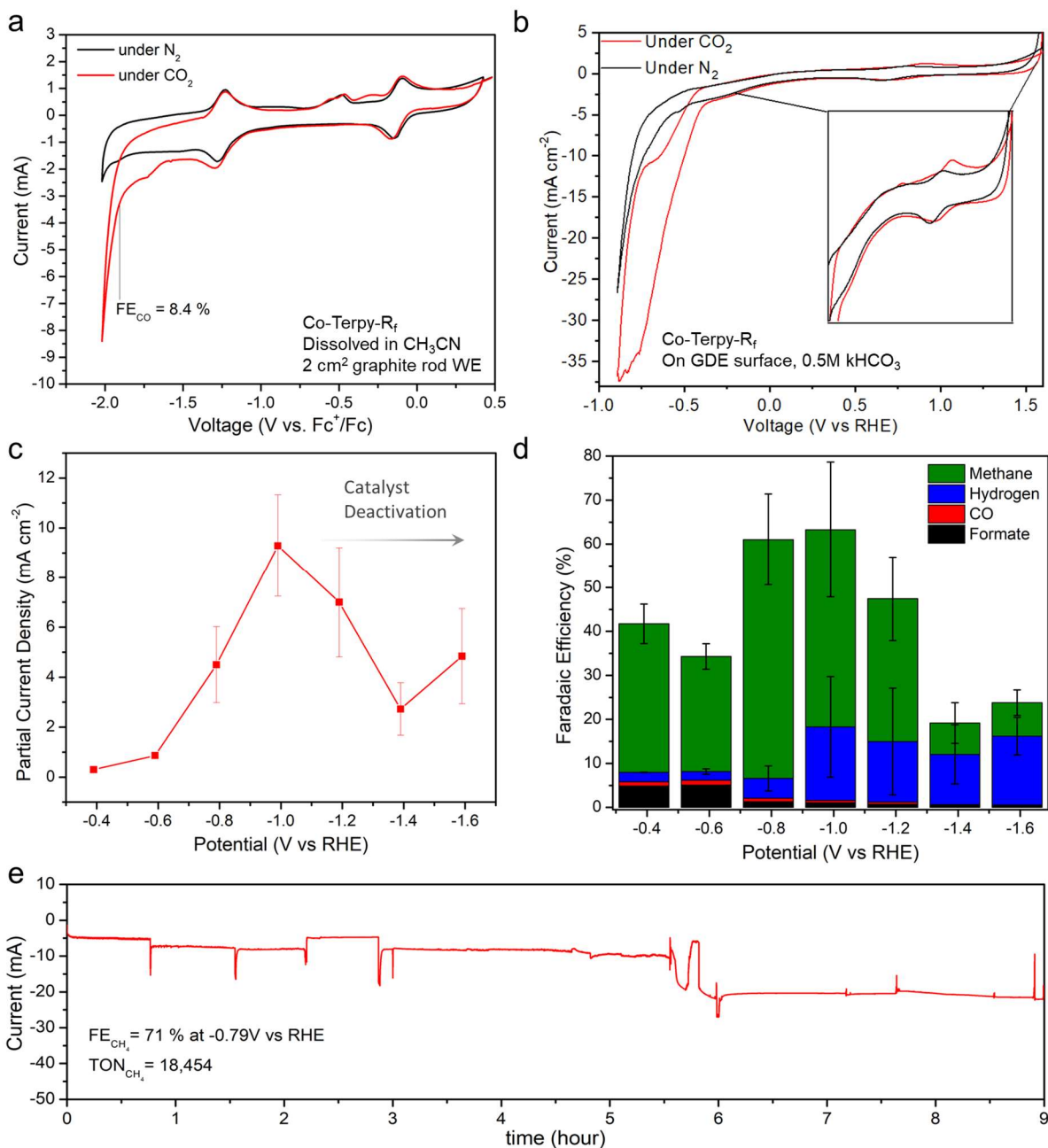

Figure 3. Cyclic voltammogram at 20 mV/s of Co Terpy-R_F dissolved in CH_3CN under N_2 and CO_2 (a). Cyclic voltammogram of Co Terpy-R_F deposited on a GDE surface with an aqueous $KHCO_3$ electrolyte, partial current density for CH_4 production (d) and FE for the production of all detected products (d). Long term stability of Co Terpy-R_F on a GDE shown by chronoamperometry at –0.79 V vs RHE (e).

The tendency to produce CH_4 was intriguing as Co polypyridine catalysts were only noted to produce formate or CO in previous studies, including in our own test of homogeneous Co Terpy-R_F in CH_3CN. In fact, electrocatalytic CH_4 production by any molecular catalyst is rare.[16,29-35] We first compared several analogous Co terpyridine catalysts in our GDE setup (Fig. 4a). Co Terpy-OH on the GDE surface only produced CO at less than 1% FE. Co Terpy-R (R=decyl, $C_{10}H_{21}$) with non-fluorinated alkyl chains, on the other hand, did give a noticeable amount of CH_4 at approx. 10% FE, however still far below the FE seen with Co Terpy-R_F. This system would likely also feature Co Terpy units within a hydrophobic pocket and similar redox behaviour (Fig. S18), but without the high degree of ordering driven by the strong perfluoro-perfluoro interactions in the Co Terpy-R_F system. This indicated that both a hydrophobic environment and ordered molecular assembly are important for CH_4 production. Interestingly, using an equivalent amount of $CoCl_2$ also gave small amounts of CH_4. Other controls such as carrying out the reaction in the absence of Co Terpy-R_F or CO_2 did not give measurable CH_4 production.

We utilized infrared spectroscopy to detect potential reaction intermediates en route to CH_4 production to derive a mechanistic explanation for the observed selectivity of Co Terpy-R_F.[36,37] Using the system at open circuit conditions as a background, we noted bands at 1650 and 2640 cm^{-1} under CO_2R conditions (Fig. S19-20). These bands match C=O and C-H vibrational modes and their presence indicates a buildup of CH_xO_y species that are produced downstream of the CO intermediate. The CO intermediate was not seen. This may point to the reduction of adsorbed CO_2 and CO, established species en route to CH_4 production,[38] as being relatively facile compared to the final steps in the reaction process such as C-O cleavage or C/O hydrogenation. This is also supported by the lack of significant CO produced from this system. Since CO_2R to CH_4 is an 8 e^-/8 H^+ process, there must be a route for proton transfer to the catalytic sites within the hydrophobic assembly and we began to suspect that there was another mechanism of H^+ transfer beyond the simple diffusion of water molecules.

To provide further insights to this hypothesis, Raman spectroscopy was used to investigate the dynamics of the Co Terpy-R_F catalyst. A particular point of interest was pyridine units that typically feature a pKa below the neutral pH of the electrolyte.[39] Thus, we concentrated on the band around 1020 cm^{-1} that corresponds to a ring breathing mode and is sensitive to both the hydrogen bonding environment and protonation of the pyridine unit (Fig. 4c, S21).[40] First, using Co Terpy-OH as a starting point, we noted that the dried molecule has only one band, centered at 1029 cm^{-1}. Dissolved in DI water, the same molecule features two bands, at 1029 and 1017 cm^{-1}, corresponding to non-protonated and protonated pyridine, respectively. In aqueous solution, this molecule is known to exist in a quinoid tautomeric form with a protonated pyridine.[41] Adding acid to the solution increases the protonated pyridine band at 1017 cm^{-1} while adding base instead results in only the non-protonated pyridine at 1029 cm^{-1} being visible. For Co Terpy-R_F, a dried film shows a single band at 1024 cm^{-1} we attribute to a pyridine coordinated to Co. With an acid solution overtop of the film, the band shifts to 1033 cm^{-1} which likely indicates a degree of a protonation to the pyridine, while with a basic solution overtop of the film, the band shifts to 1024 cm^{-1} as there is no more protonated pyridine. Interestingly, under CO_2R conditions using a GDE-based spectroelectrochemical cell, the band splits into two – a main band at 1019 cm^{-1} and a shoulder at 1033 cm^{-1}. We take this to signify that the terpyridine unit of Co Terpy-R_F is partially protonated in these conditions. In particular, in the Co(I) oxidation state, binding to 6 pyridine N

atoms is no longer favorable and one pyridine unit will dissociate, further promoting its protonation as well as leaving the Co site open for catalysis. As pyridine units have facilitated proton conductivity in previous studies,[42,43] and proton shuttles in CO_2 reduction[44] it is not unreasonable to think that they can be playing a similar role within the self-assembled films. This is also evident in the weak proton conductivity of Co Terpy-R_F films (Fig. S23).

To more precisely probe whether proton shuttling could be in play, we turned to proton inventory studies, an experimental technique that elucidates this behaviour by measuring catalytic activity as a function of electrolyte deuteration.[44-46] Here, the relative activity of a catalytic system in a deuterated solvent, which is measured through current density, j_n, is plotted relative to its activity in a fully protonated solvent, j_0. Thus, j_n/j_0 can be modelled through a modified Gross-Butler equation:

$j_n=j_0(1−n+n\phi)Z^n$:

where n is the fractional deuteration:

$$n = \frac{[D_2O]}{[D_2O] + [H_2O]}$$

ϕ denotes the isotopic fractionation parameter that signifies the tendency of a hydrogenic site acting as a proton shuttle to exchange with D^+ relative to H^+ and Z is the number of hydrogenic sites functioning as proton relays. If proton shuttling is in place, a plot of j_n/j_0 vs. n will show a slightly parabolic relationship and the data can be modelled with $Z > 1$. In contrast, if there is no shuttling in place, there will be a linear j_n/j_0 vs. n curve and $Z = 1$. Proton inventory experiments on the Co Terpy-R_F illustrated that under catalytic conditions, the data set can be fitted to an equation with $\phi = 0.61$ and $Z = 1.26$ (Fig. 4d). In contrast, conducting the same experiment just positive of the Co(II/I) redox couple, where proton shuttling is not expected to be in play, yielded a fit of ϕ and $Z = 1$ (Fig. S22).

Thus, we come to a possible mechanism in which the self-assembled Co Terpy-R_F molecules create a hydrophobic environment on the GDE surface (Fig. 4e). This is ideal in allowing CO_2 permeation directly from the gas phase and electron transfer from the electrode. At the same time, protons may transfer not directly through free water but, at least in part, via a pyridine-assisted proton conduit and specific channels within these structured films and this acts to hydrogenate the CO_2R intermediates. Proton conduction has previously been implicated within MOFs that accelerated their performance towards hydrogen evolution.[47] Further, the catalytic mechanism proposed bears similarity to observations of ligand-assisted protonation in CO_2 methanation in molecular[48] and heterogeneous[49] systems, as well as terpyridine units playing the same role in CO_2R to CO[20]; proton channels are also a key factor in the performance of CO_2-reducing enzymes.[50] The creation of a hydrophobic pocket stabilizes CO and other CO_2R intermediates for further hydrogenation all the way to the CH_4 final product and is an example of environment-dictated electrocatalysis. This is in line with previous work highlighting the

beneficial effects of increased hydrophobicity on the multi-electron reduction of CO_2,[13,51,52] as well as the impact of substrate diffusion in the catalyst environment[53] on its performance.
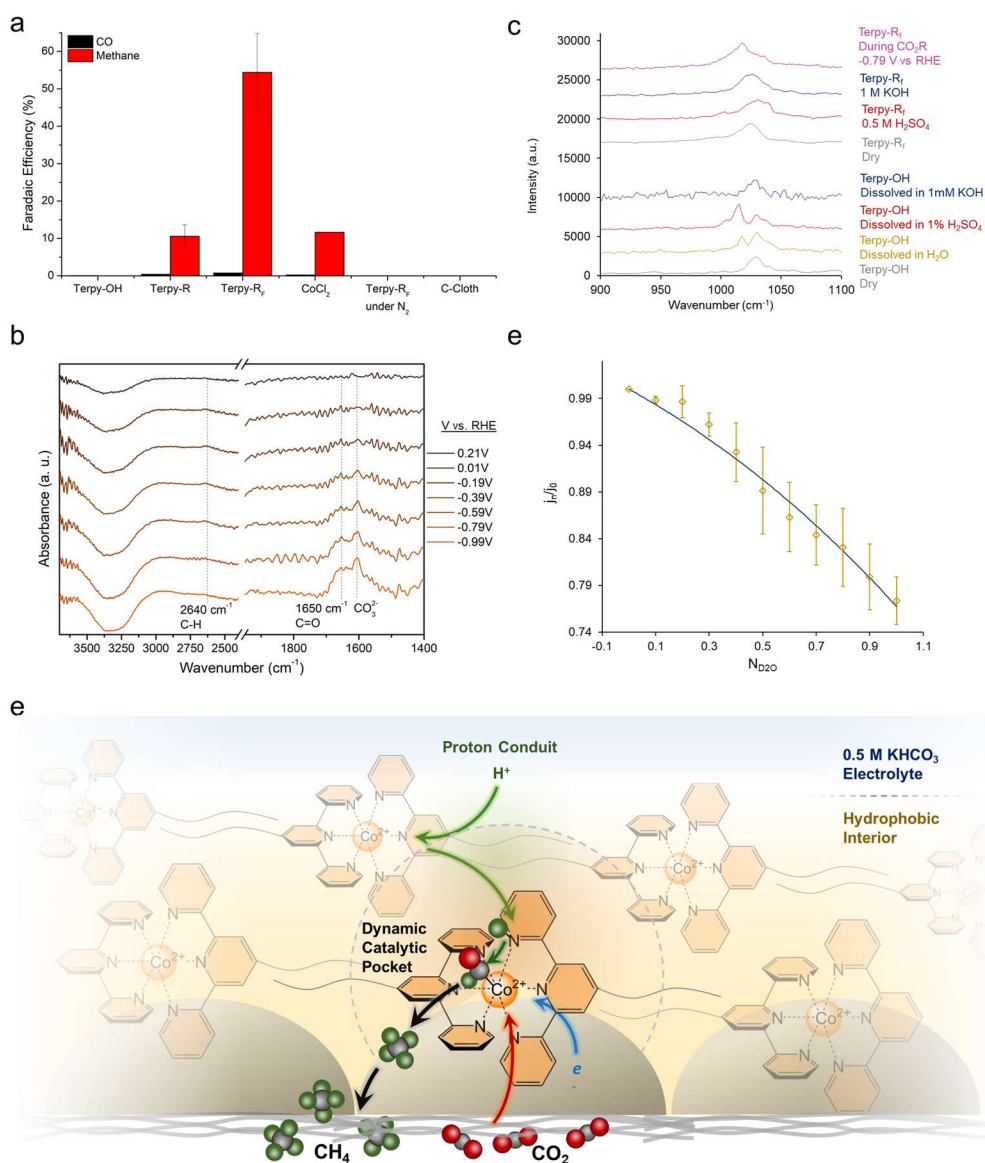

Figure 4. CO_2R on Co Terpy-R_F and control samples (a). Reaction intermediates are detected with IR spectroscopy (b) and the catalyst protonation via Raman spectroscopy (c). Proton inventory studies (d) point to the presence of proton shuttling in the system. The data together lead to a possible mechanism in which a terpyridine-based proton conduit hydrogenates the reaction intermediates within a hydrophobic catalytic pocket (e).

As a last endeavor, we moved to demonstrate a possible route for optimizing the system by taking advantage of the perfluorinated side chains and their strong interaction with other fluorinated species. A challenge we encountered with Co Terpy-R_F was that only 1% of the total immobilized catalyst was 'wired' to the electrode, as quantified through integrating the Co(II/III)

redox wave. To enhance the catalyst wiring, we added fluorinated carbon nanotubes (F-CNTs) into the catalyst dispersion prior to drop casting it onto the GDE (Fig. 5a and S24-25). A CV of the system under CO_2R flow showed enhanced waves of the Co(III/II) and Co(II/I) redox couples despite using the same catalyst concentration (Fig. 5b), indicative of better electrical connection to the electrode via the F-CNT electron conduits. Measuring the CO_2R reactivity showed both an enhanced CH_4 FE of up to 80% (Fig. 5c and S26) and an increased CH_4 partial current density of 10 mA cm^{-2} (Fig. 5d) at –0.79 V vs. RHE. Finally, using an electrolyzer in flow, the catalyst displayed constant CH_4 production over a period of 9 hours at –0.59 V vs. RHE (Fig. 5e and S27). Variations in FE may originate from changes in wetting and hydration of the gas-liquid-solid interface over time. While the system is still far from optimized, such experiments present a viable route forward towards attaining industrially relevant current densities of 200 mA cm^{-2} or more. This performance particularly stands out amongst Co Terpy molecular electrocatalysts or those adsorbed onto GDEs reported to date, both of which tend to be selective for CO.
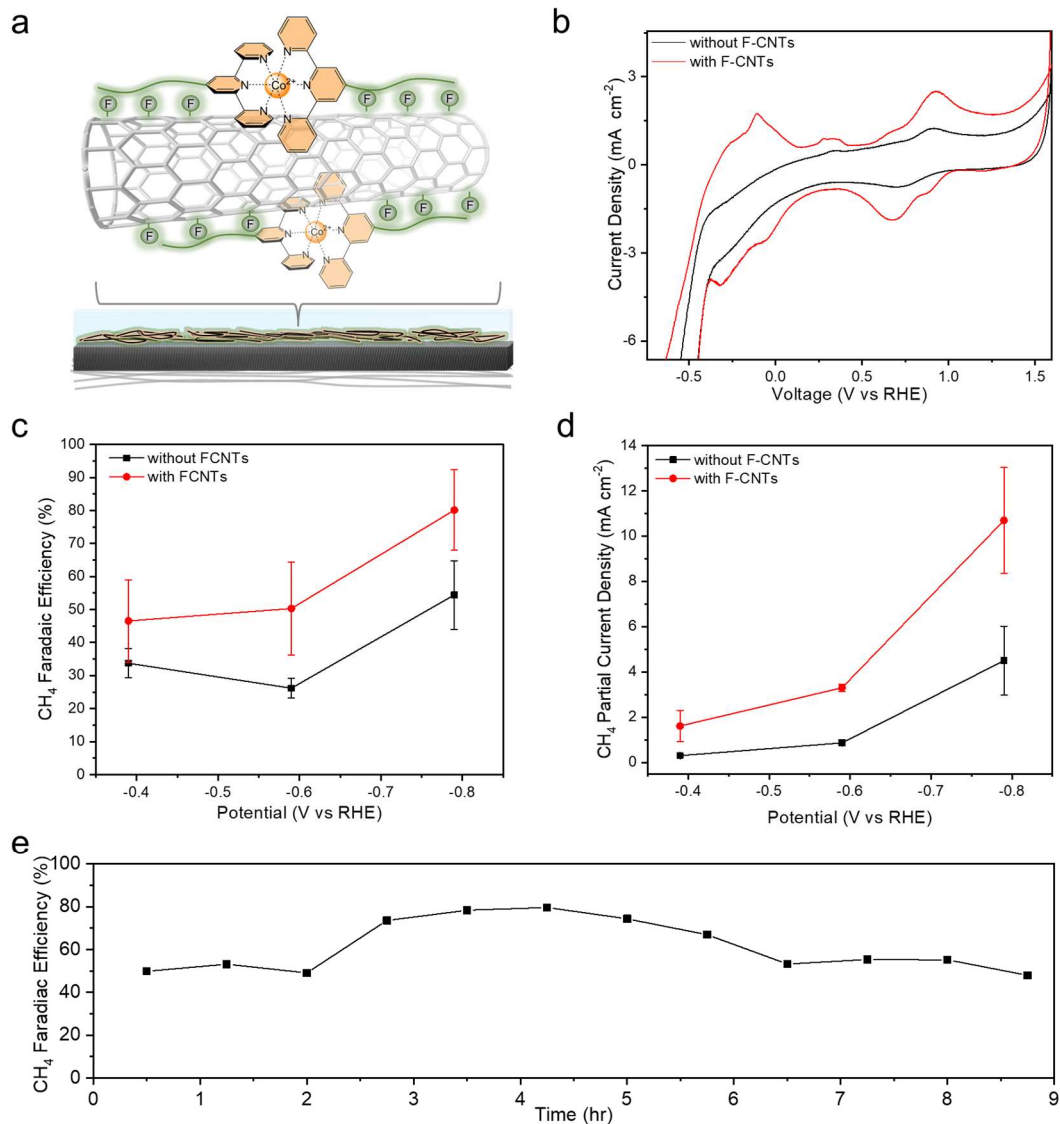
Figure 5. Improvement of the electrical connection of Co Terpy-R_F to the carbon cloth electrode upon incorporation of fluorinated carbon nanotubes (F-CNTs) (a). Increased electrochemical response (b), CH_4 FE (c) and partial current density (d) of Co Terpy-R_F in the presence of F-CNTs. Consistent CH_4 production over time at -0.59 V vs. RHE (e).

Concluding Remarks

In summary, we present a system comprised of a molecular Co Terpy-R_F catalyst that assembles via hydrophobic interactions through perfluorinated side chains. The hydrophobicity was leveraged to integrate these species into a GDE in which the hydrophobicity is an inherent advantage rather than obstacle. The unique reaction environment within these Co Terpy-R_F layers shifted the CO2R selectivity to CH_4, which reached up to 80% in an optimized system. Mechanistic

investigations suggest that the hydrophobic catalytic pocket stabilizes CO_2R intermediates while a pyridine-assisted proton conduit acts to shuttle protons to the active sites and hydrogenate the intermediates en route to the CH_4 final product. These findings pave the way towards the use of functional catalytic environments that dictate electrocatalytic behaviour and enable access to new reactivity.

Conflicts of interest

The authors declare no competing interests.

Acknowledgements

References

1   Stephens, I. E. *et al.* 2022 roadmap on low temperature electrochemical CO2 reduction. *J. Phys.: Energy* **4**, 042003 (2022).

2   Bushuyev, O. S. *et al.* What Should We Make with CO2 and How Can We Make It? *Joule* **2**, 825-832 (2018).

3   Chen, A. & Lin, B.-L. A Simple Framework for Quantifying Electrochemical CO2 Fixation. *Joule* **2**, 594-606 (2018).

4   Kibria Nabil, S., McCoy, S. & Kibria, M. G. Comparative life cycle assessment of electrochemical upgrading of CO2 to fuels and feedstocks. *Green Chem.* **23**, 867-880 (2021).

5   Ross, M. B. *et al.* Designing materials for electrochemical carbon dioxide recycling. *Nat. Catal.* **2**, 648-658 (2019).

6   Birdja, Y. Y. *et al.* Advances and challenges in understanding the electrocatalytic conversion of carbon dioxide to fuels. *Nat. Energy* **4**, 732-745 (2019).

7   Benson, E. E., Kubiak, C. P., Sathrum, A. J. & Smieja, J. M. Electrocatalytic and homogeneous approaches to conversion of CO2 to liquid fuels. *Chem. Soc. Rev.* **38**, 89-99 (2009).

8   Takeda, H., Cometto, C., Ishitani, O. & Robert, M. Electrons, Photons, Protons and Earth-Abundant Metal Complexes for Molecular Catalysis of CO2 Reduction. *ACS Catal.* **7**, 70-88 (2017).

9   Sun, L., Reddu, V., Fisher, A. C. & Wang, X. Electrocatalytic reduction of carbon dioxide: opportunities with heterogeneous molecular catalysts. *Energy Environ. Sci.* **13**, 374-403 (2020).

10   Corbin, N., Zeng, J., Williams, K. & Manthiram, K. Heterogeneous molecular catalysts for electrocatalytic CO2 reduction. *Nano Res.* **12**, 2093-2125 (2019).

11   Weekes, D. M., Salvatore, D. A., Reyes, A., Huang, A. & Berlinguette, C. P. Electrolytic CO2 Reduction in a Flow Cell. *Acc. Chem. Res.* **51**, 910-918 (2018).

12   Liang, H.-Q. *et al.* Hydrophobic Copper Interfaces Boost Electroreduction of Carbon Dioxide to Ethylene in Water. *ACS Catal.* **11**, 958-966 (2021).

13   Xing, Z., Hu, L., Ripatti, D. S., Hu, X. & Feng, X. Enhancing carbon dioxide gas-diffusion electrolysis by creating a hydrophobic catalyst microenvironment. *Nat. Commun.* **12**, 136 (2021).

14   Ren, S. *et al.* Molecular electrocatalysts can mediate fast, selective CO2 reduction in a flow cell. *Science* **365**, 367-369 (2019).

15   Wang, M. *et al.* CO2 electrochemical catalytic reduction with a highly active cobalt phthalocyanine. *Nat. Commun.* **10**, 3602 (2019).

16   Furuya, N. & Matsui, K. Electroreduction of carbon dioxide on gas-diffusion electrodes modified by metal phthalocyanines. *J. Electroanal. Chem. Interfac. Chem.* **271**, 181-191 (1989).

17   Jiang, Z. *et al.* Molecular Catalyst with Near 100% Selectivity for CO2 Reduction in Acidic Electrolytes. *Adv. Energy Mater.* **n/a**, 2203603 (2022).

18   Sun, L. *et al.* Cobalt Quaterpyridine Complexes for Highly Efficient Heterogeneous CO2 Reduction in Aqueous Media. *Adv. Energy Mater.* **12**, 2202108 (2022).

19   Siritanaratkul, B. *et al.* Zero-Gap Bipolar Membrane Electrolyzer for Carbon Dioxide Reduction Using Acid-Tolerant Molecular Electrocatalysts. *J. Am. Chem. Soc.* **144**, 7551-7556 (2022).

20   Leung, J. J. *et al.* Solar-driven reduction of aqueous CO2 with a cobalt bis(terpyridine)-based photocathode. *Nat. Catal.* **2**, 354-365 (2019).

21   Pati, P. B. *et al.* Photocathode functionalized with a molecular cobalt catalyst for selective carbon dioxide reduction in water. *Nat. Commun.* **11**, 3499 (2020).

22   Ahmed, M. E., Rana, A., Saha, R., Dey, S. & Dey, A. Homogeneous Electrochemical Reduction of CO2 to CO by a Cobalt Pyridine Thiolate Complex. *Inorg. Chem.* **59**, 5292-5302 (2020).

23   Dey, S., Todorova, T. K., Fontecave, M. & Mougel, V. Electroreduction of CO2 to Formate with Low Overpotential using Cobalt Pyridine Thiolate Complexes. *Angew. Chem. Int. Ed.* **59**, 15726-15733 (2020).

24   Elgrishi, N., Chambers, M. B. & Fontecave, M. Turning it off! Disfavouring hydrogen evolution to enhance selectivity for CO production during homogeneous CO2 reduction by cobalt–terpyridine complexes. *Chem. Sci.* **6**, 2522-2531 (2015).

25   Tatikonda, R., Bhowmik, S., Rissanen, K., Haukka, M. & Cametti, M. Metallogel formation in aqueous DMSO by perfluoroalkyl decorated terpyridine ligands. *Dalton Trans.* **45**, 12756-12762 (2016).

26   Baker, R. J., Colavita, P. E., Murphy, D. M., Platts, J. A. & Wallis, J. D. Fluorine–Fluorine Interactions in the Solid State: An Experimental and Theoretical Study. *J. Phys. Chem. A* **116**, 1435-1444 (2012).

27   Ferreira, H., Conradie, M. M. & Conradie, J. Electrochemical and electronic properties of a series of substituted polypyridine ligands and their Co(II) complexes. *Inorg. Chim. Acta* **486**, 26-35 (2019).

28   Bredar, A. R. C., Chown, A. L., Burton, A. R. & Farnum, B. H. Electrochemical Impedance Spectroscopy of Metal Oxide Electrodes for Energy Applications. *ACS Appl. Energy Mater.* **3**, 66-98 (2020).

29   Shen, J. *et al.* Electrocatalytic reduction of carbon dioxide to carbon monoxide and methane at an immobilized cobalt protoporphyrin. *Nat. Commun.* **6**, 8177 (2015).

30   Ahmed, M. E. *et al.* Repurposing a Bio-Inspired NiFe Hydrogenase Model for CO2 Reduction with Selective Production of Methane as the Unique C-Based Product. *ACS Energy Lett.* **5**, 3837-3842 (2020).

31   Boutin, E. & Robert, M. Molecular Electrochemical Reduction of CO2 beyond Two Electrons. *Trends Chem.* **3**, 359-372 (2021).

32   Furuya, N. & Koide, S. Electroreduction of carbon dioxide by metal phthalocyanines. *Electrochim. Acta* **36**, 1309-1313 (1991).

33   Abdinejad, M. *et al.* Electrocatalytic Reduction of CO2 to CH4 and CO in Aqueous Solution Using Pyridine-Porphyrins Immobilized onto Carbon Nanotubes. *ACS Sustain. Chem. Eng.* **8**, 9549-9557 (2020).

34   Dong, S.-T., Xu, C. & Lassalle-Kaiser, B. Multiple C–C bond formation upon electrocatalytic reduction of CO2 by an iron-based molecular macrocycle. *Chem. Sci.* (2023).

35   Weng, Z. *et al.* Electrochemical CO2 Reduction to Hydrocarbons on a Heterogeneous Molecular Cu Catalyst in Aqueous Solution. *J. Am. Chem. Soc.* **138**, 8076-8079 (2016).

36   Heidary, N., Ly, K. H. & Kornienko, N. Probing CO2 Conversion Chemistry on Nanostructured Surfaces with Operando Vibrational Spectroscopy. *Nano Lett.* **19**, 4817-4826 (2019).

37   Zhu, S., Li, T., Cai, W.-B. & Shao, M. CO2 Electrochemical Reduction As Probed through Infrared Spectroscopy. *ACS Energy Lett.* **4**, 682-689 (2019).

38   Peterson, A. A. & Nørskov, J. K. Activity Descriptors for CO2 Electroreduction to Methane on Transition-Metal Catalysts. *J. Phys. Chem. Lett.* **3**, 251-258 (2012).

39   Nazeeruddin, M. K., Zakeeruddin, S. M., Humphry-Baker, R., Kaden, T. A. & Grätzel, M. Determination of pKa Values of 4-Phosphonato-2,2':6',2' '-Terpyridine and Its Ruthenium(II)-Based Photosensitizer by NMR, Potentiometric, and Spectrophotometric Methods. *Inorg. Chem.* **39**, 4542-4547 (2000).

40   Wattanavichean, N., Casey, E., Nichols, R. J. & Arnolds, H. Discrimination between hydrogen bonding and protonation in the spectra of a surface-enhanced Raman sensor. *Phys. Chem. Chem. Phys.* **20**, 866-871 (2018).

41   Murguly, E., B. Norsten, T. & Branda, N. Tautomerism of 4-hydroxyterpyridine in the solid, solution and gas phases: an X-ray, FT-IR and NMR study. *J. Chem. Soc., Perkin Trans. 2*, 2789-2794 (1999).

42   Guo, Z.-C., Shi, Z.-Q., Wang, X.-Y., Li, Z.-F. & Li, G. Proton conductive covalent organic frameworks. *Coord. Chem. Rev.* **422**, 213465 (2020).

43   Yang, J. *et al.* Hydroxyl pyridine containing polybenzimidazole membranes for proton exchange membrane fuel cells. **446**, 318-325 (2013).

44   Liu, Y. & McCrory, C. C. L. Modulating the mechanism of electrocatalytic CO2 reduction by cobalt phthalocyanine through polymer coordination and encapsulation. *Nat. Commun.* **10**, 1683 (2019).

45   Liu, H. *et al.* Second Sphere Effects Promote Formic Acid Dehydrogenation by a Single-Atom Gold Catalyst Supported on Amino-Substituted Graphdiyne. *Angew. Chem. Int. Ed.* **n/a** (2023).

46   Venkatasubban, K. & Schowen, R. L. The Proton Inventory Techniqu. *Critical Reviews in Biochemistry* **17**, 1-44 (1984).

47   Hod, I. *et al.* A porous proton-relaying metal-organic framework material that accelerates electrochemical hydrogen evolution. *Nat. Commun.* **6**, 8304 (2015).

48   Nganga, J. K. *et al.* Methane Generation from CO2 with a Molecular Rhenium Catalyst. *Inorg. Chem.* **60**, 3572-3584 (2021).

49   Li, Y. *et al.* Promoting CO2 methanation via ligand-stabilized metal oxide clusters as hydrogen-donating motifs. *Nat. Commun.* **11**, 6190 (2020).

50   Gong, W. *et al.* Structure of the α2ε2 Ni-dependent CO dehydrogenase component of the Methanosarcina barkeri acetyl-CoA decarbonylase/synthase complex. *Proc. Natl. Acad. Sci. U.S.A.* **105**, 9558-9563 (2008).

51   Xue, L. *et al.* Hydrophobic 1-octadecanethiol functionalized copper catalyst promotes robust high-current CO2 gas-diffusion electrolysis. *Nano Res.* **15**, 1393-1398 (2022).

52   Wakerley, D. *et al.* Bio-inspired hydrophobicity promotes CO2 reduction on a Cu surface. *Nat. Mater.* **18**, 1222-1227 (2019).

53   Allan, M. G., McKee, M. J., Marken, F. & Kuehnel, M. F. Solvent-controlled O2 diffusion enables air-tolerant solar hydrogen generation. *Energy Environ. Sci.* **14**, 5523-5529 (2021).

Hydrophobic molecular assembly at the gas-liquid-solid interface drives highly selective CO_2 electromethanation

Morgan McKee[1], Maximilian Kutter[2,3], Dieter Lentz[4], Moritz F. Kühnel[2,5]* and Nikolay Kornienko[1]*

[1]Department of Chemistry, Université de Montréal, 1375 Ave. Thérèse-Lavoie-Roux, Montréal, QC H2V 0B3, Canada

[2]Department of Chemistry, Swansea University, Singleton Park, Swansea SA2 8PP, Wales, UK

[3]Electrochemical Process Engineering, Universität Bayreuth, Universitätsstraße 30, 95447 Bayreuth, Germany

[4]Freie Universität Berlin, Institut für Chemie und Biochemie – Anorganische Chemie, Fabeckstraße 34-36, 14195 Berlin, Germany

[5]Fraunhofer Institute for Wind Energy Systems IWES, Am Haupttor BC 4310, 06237 Leuna, Germany

*Correspondence to: m.f.kuehnel@swansea.ac.uk and nikolay.kornienko@umontreal.ca

Experimental procedures

Synthesis of 4'-((4,4,5,5,6,6,7,7,8,8,9,9,9-tridecafluorononyl)oxy)- 2,2':6',2''- terpyridine (terpy-R$_F$)[25]

4'-hydroxy-2,2':6',2''-terpyridine (125 mg, 0.5 mmol), 18-crown-6 (catalytic amount) and K_2CO_3 (207 mg, 1.5 mmol) in acetone (30 mL) was stirred at room temperature for 1 h. Once stirred, 1H,1H,2H,2H,3H,3H-perfluoroundecyl iodide (295 mg, 0.5 mmol) in acetone (2 mL) was added dropwise to the reaction mixture at room temperature and resulting mixture was then refluxed for 48 h. After that, the reaction was quenched with water (20 mL) and extracted with DCM (3 × 20 mL). Once extracted, the solvent was evaporated off to give a yellow solid which was then recrystallized in hot ethanol to produce white crystals (255 mg, 0.36 mmol, 72%).

^{1}H NMR (400 MHz, CDCl$_3$) δ: 8.74 (d, 2H, J = 4.3 Hz); 8.69 (d, 2H, J = 7.5 Hz); 8.14 (s, 2H); 7.93 (t, 2H, J = 6.7 Hz); 7.41 (t, 2H, J = 5.5 Hz); 4.38 (t, 2H, J = 5.5 Hz); 2.36 (m, 2H); 2.2 (m,

2H) ppm. ^{19}F NMR (400 MHz, CDCl$_3$) δ: -80.72 (t, 3F, J = 9.9 Hz); -114.30 (m, 2F); -121.74 (d, 6F); -122.66 (s, 2F); -123.32 (s, 2F); -126.05 (m, 2F) ppm.

Synthesis of terpy-R

4'-hydroxy-2,2':6',2"-terpyridine (50 mg, 0.2 mmol), 18-crown-6 (catalytic amount, 10 mg) and K$_2$CO$_3$ (83 mg, 0.6 mmol) in acetone (10 mL) was stirred at room temperature for 1 h. Once stirred, 1H,1H,2H,2H,3H,3H-1-iododecane (295 mg, 0.2 mmol) in acetone (1 mL) was added dropwise to the reaction mixture at room temperature and resulting mixture was then refluxed for 48 h. After that, the reaction was quenched with water (8 mL) and extracted with DCM (3 × 15 mL). Once extracted, the solvent was evaporated off to give a precipitate which was then recrystallized in hot ethanol to produce white crystals (35 mg, 0.09 mmol, 45%).

^{1}H NMR (400 MHz, CDCl$_3$) δ: 8.69 (d, 2H, J = 4.78 Hz); 8.61 (d, 2H); 8.01 (s, 2H); 7.84 (t, 2H, J = 10.2 Hz); 7.32 (t, 2H); 4.22 (t, 2H, J = 6.5 Hz); 1.85 (m, 2H); 2.50 (m, 2H), 1.28 (m, 12H), 0.88 (t, 3H, J = 6.8 Hz) ppm.

Synthesis of terpyridine complexes

A 10 mM solution of cobalt chloride hexahydrate or Co (II) tetrafluoroborate hexahydrate in methanol was added to a 20 mM solution of terpyridine ligand in methanol. The mixture was then sonicated for 15 minutes to produce an orange solution which was used without further purification as a solution, or the solvent was evaporated for product characterisation.

[Co(terpy-R$_F$)$_2$](BF$_4$)$_2$: HRMS (ESI): m/z: 738.5670 (M$^{+•}$ calc.:738.5682). **IR** (ATR) $\tilde{v}$: 3092 (w), 1616 (m), 1603 (m), 1571 (w), 1559 (w), 1473 (m), 1441 (m), 1406 (w), 1365 (m), 1202 (s), 1147 (s), 1116 (m), 1057 (s), 1032 (s), 866 (w), 827 (w), 795 (s), 748 (m), 729 (m), 705 (m), 657 (m), 624 (m), 606 (w), 581 (w), 572 (w), 560 (w), 540 (w) cm^{-1}.

[Co(terpy-R$_F$)$_2$](BF$_4$)$_2$ crystals for single crystal X-ray structural analysis were obtained by slow evaporation of methanol at 4 °C

Adsorption of Co Terpy-R$_F$ onto ITO

ITO-coated glass slides were cleaned in a mixture of H_2O_2:NH_3:H_2O (1:1:5) for 1 h at 70 °C, washed with deionized water and dried before being placed in a MeOH solution of (1H,1H,2H,2H-heptadecafluorodec-1-yl)phosphonic acid (10 mM) for 24 h. The slides were washed with MeOH, dried and placed in a MeOH solution of [Co(terpy-R$_F$)$_2$](BF$_4$)$_2$ (10 mM) for 24 h. Afterwards, the slides were rinsed with MeOH and dried in air.

Characterization

Single-crystal X-ray crystallography

Structure determination was performed on a Bruker D8 Venture system at 100 K. The data sets were collected using APEX3, were refined and reduced with SAINT and solved with SHELXT. All programs were provided by Bruker. See table S1 for details. Crystalmaker and Mercury 3.10 were used for the structure visualization and to render images. Where shown, thermal ellipsoids are drawn at a 50 % probability level.

X-ray photoelectron spectroscopy (XPS)

XPS was recorded on a Kratos Analytical spectrometer using a monochromated Al Kα X-ray source at a power of 225 W and using the integral charge neutralizer. Data was acquired with a pass energy of 20 eV and a step size of 0.1 eV. Data was analyzed with CasaXPS (version 2.3.17dev6.4k), using the Kratos RSF library and Shirley backgrounds.

Electrochemistry and product quantification

Cyclic voltammetry (CV) was accomplished using a Bio-Logic SP-200 Potentiostat (BioLogic Science Instruments, France). A three-electrode system has been employed by applying the carbon

cloth gas diffusion layer (GDL-CT (W1S1009, Fuel Cells Etc.) as the working electrode, Ag/AgCl as the reference electrode and a glassy carbon rod as the counter electrode. Additionally, a homogeneous system was also employed using two glassy carbon rods as the working electrode and counter electrode and Ag wire as a pseudo-reference which was corrected using ferrocene. In this case, the electrolyte was $TBAPF_6$ (0.1 M) in acetonitrile where 1 mM of the catalyst was dissolved.

The preparation of working electrode followed steps: $CoCl_2 \bullet 6H_2O$ (2.37 mg, 10 μmol) and terpyridine ligand (20 μmol) was added to 2 mL MeOH. After ultrasonic mixing for 15 minutes, 200 μL of the catalyst ink was dropped onto the carbon cloth and allowed to dry. This led to a catalyst loading of approximately 3 mg/cm^2. 0.5 M $KHCO_3$ solution was used as the electrolyte in all measurements. The CVs were measured in the range of 1.6 ~ –0.98 V (vs. RHE) at a sweep rate of 20 mVs^{-1}. Potentiostatic electrolysis was conducted in a gas diffusion electrode (GDE) cell. Before each electrolysis experiment, 1 mL electrolyte was added into the cell, the flow rate of CO_2 is 10 mL/min. All reactions were carried out at room temperature (23 ± 1 °C).

In order to quantify the products of the reaction, gas chromatography (GC, SRI 8610C) and NMR (Bruker AVANCE II 400 se) were performed to reveal the content and composition of the gas and liquid products respectively. A sealed GDE cell was used and connected with the GC. The CO_2 flow rate employed was 10 mL/min and the products were probed in flow mode as the outlet from the GDE cell flowed directly through the GC. For NMR analysis, 300 μL liquid electrolyte after an electrolysis run was mixed with 400 μL D_2O to quantify liquid products. For NMR measurements, products were quantified using DMSO as an internal standard and calibration curves for products in the liquid phase (Fig. S4). Gaseous products were similarly quantified through the integration of peak area corresponding to various products, which were first measured with a series of calibration curves (H_2, CO, CH_4). The GC measurements were also collected in flow mode at 10 SCCM CO_2 flow with N_2 as the carrier gas in the GC. Typically, liquid products were acquired after 30 minutes of electrolysis.

Proton inventory studies were conducted with a phosphate-buffered solution (0.5M, pH/pD 5). The pH and pD of both solutions were set equal using the relationship of pD = pH$_{meter reading}$ + 0.4. Steady state currents were recorded in solutions of varying deuteration by making mixtures of set ratios from the protonated and deuterated stock solutions. Currents were recorded once steady state

values were attained (approx. 1 min) on the same electrode by progressively changing the electrolyte from completely protonated to fully deuterated.

Proton conductivity measurements were performed by dropcasting a solution of Co Terpy-R$_F$ onto a glass slide, into an O-ring that fixed the deposition area. After drying, electrical contacts were made with copper tape, 2 mm apart. A second glass slide was put overtop and the two slides pressed against each other with lab clamps. Conductivity was measured through impedance measurements at open circuit from 1 Hz to 100 kHz with 10 mV perturbations. Ambient temperature (298K) and relative humidity (30%) was used for preliminary measurements.

Faradaic efficiency and turnover number

The Faradaic efficiency (FE) was calculated by using the following formula:

$$FE = \frac{nZF}{Q}$$

Where n is the moles of product, z is the number of electrons exchanged, F is Faraday's constant (96485 C mol^{-1}) and Q the total charge passed during the reaction

Turnover number was calculated using the following equation:

$$TON = \frac{n_{produ}}{n_{electroactive\ species}}$$

The number of moles of electroactive species was determined through cyclic voltammetry.

In-situ infrared (IR) spectroscopy

IR spectra were acquired on a ThermoFischer Nicolet 380 FTIR-ATR with a ZnSe ATR crystal that was coated with a diamond surface. Typically, 200 scans were acquired for each measurement. A three-electrode GDE cell was used for the in-situ IR experiment. Cu wire was used as counter electrode, Ag/AgCl was used as reference, the above carbon cloth with a Co terpy complex as working electrode. The electrolyte employed was 0.5 M KHCO$_3$ under a constant CO$_2$ gas flow. The catalyst, deposited onto a carbon cloth gas diffusion electrode was facing downwards towards the ATR crystal, with a thin electrolyte layer between. The working electrode was gently pressed with a porous foam stud so that there was still ample gas permeation into the triple-phase boundary that was being probed with the IR evanescent wave.

Raman Spectroscopy

Raman Spectra were collected using a Renishaw Invia system with a 514 nm laser having a 5 mW output power. The laser line focus illumination technique was used that spread the laser intensity out over a line and minimized the power concentrated at any one spot. The spectra were collected at full intensity power and a typical collection time was 60 seconds. A water immersion objective (numerical aperture of 0.7, working distance of 1 mm) was used to maximize signal intensity. Raman measurements were performed in a standard 3-electrode configuration instead of adapting to a gas-diffusion electrode as an initial test. For operando Raman measurements, a Ag/AgCl reference electrode and a Ni foam counter electrode was used. A 0.5 M $KHCO_3$ electrolyte under constant CO_2 or N_2 flow was also used. The working electrode consisted of the same Co terpy complex loaded onto a carbon cloth electrode.

Figure S1. ^{1}H NMR spectra of Terpy-R$_F$.

Figure S2. ^{19}F NMR spectra of Terpy-R$_F$.
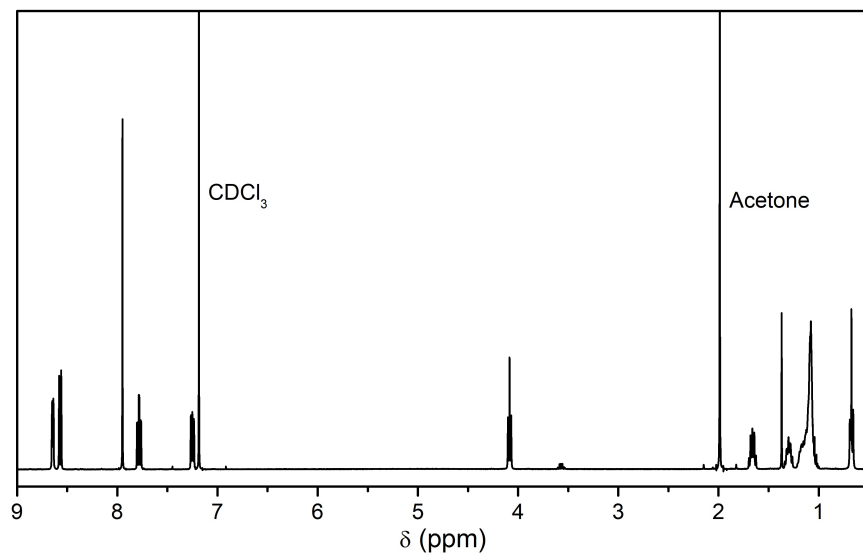
Figure S3. ^{1}H NMR spectra of Terpy-R.
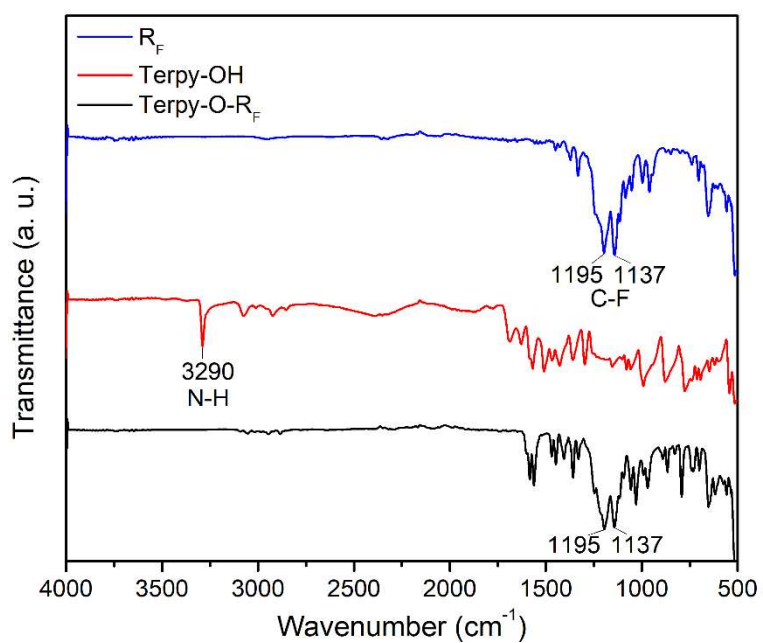
Figure S4. FTIR spectrum of Terpy-R$_F$ and corresponding starting material.
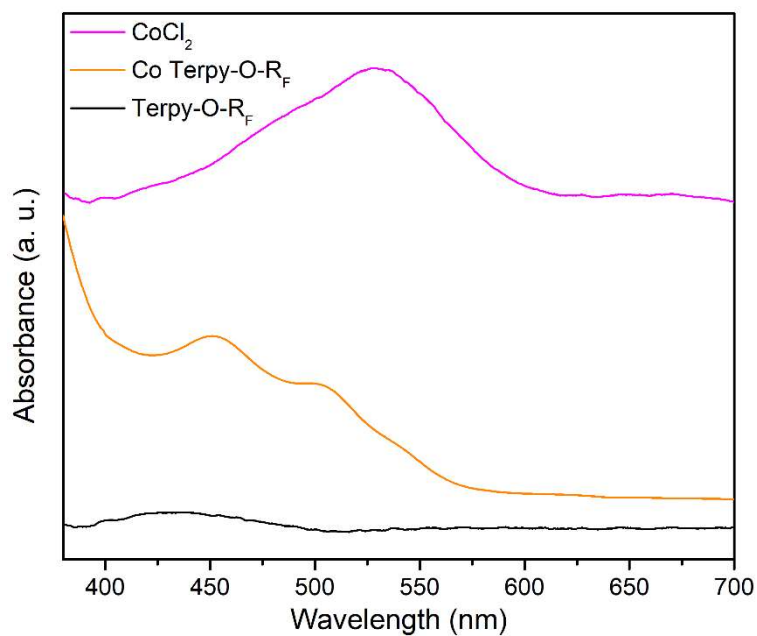
Figure S5. UV-Vis absorption spectrum of Terpy-R_F, Co Terpy-R_F and $CoCl_2$ in MeOH.
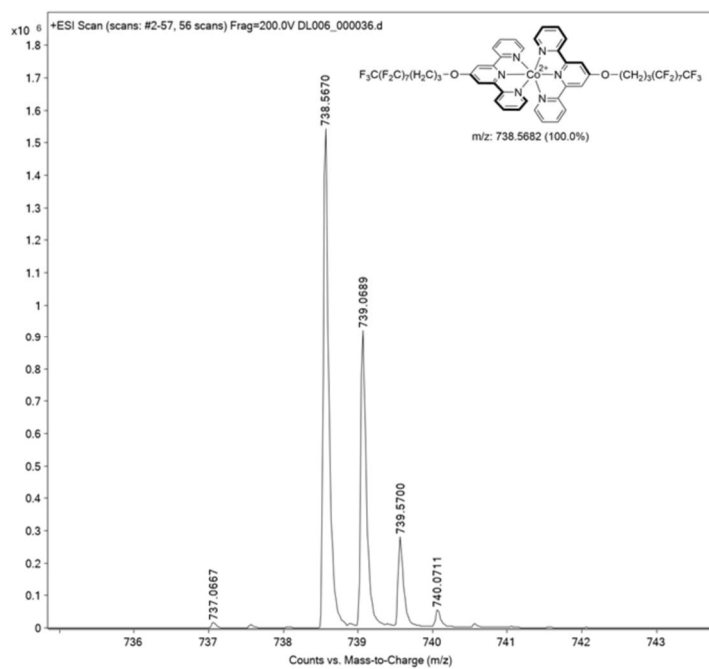
Figure S6. High-resolution mass spectrometric analysis of Co Terpy-R_F matches the expected m/z ratio.
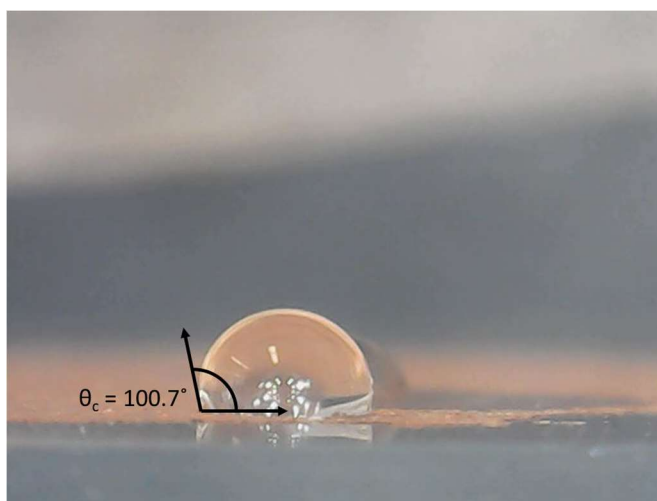
Figure S7. Contact angle measurements of a Co Terpy-R$_F$ film dried onto a glass slide.
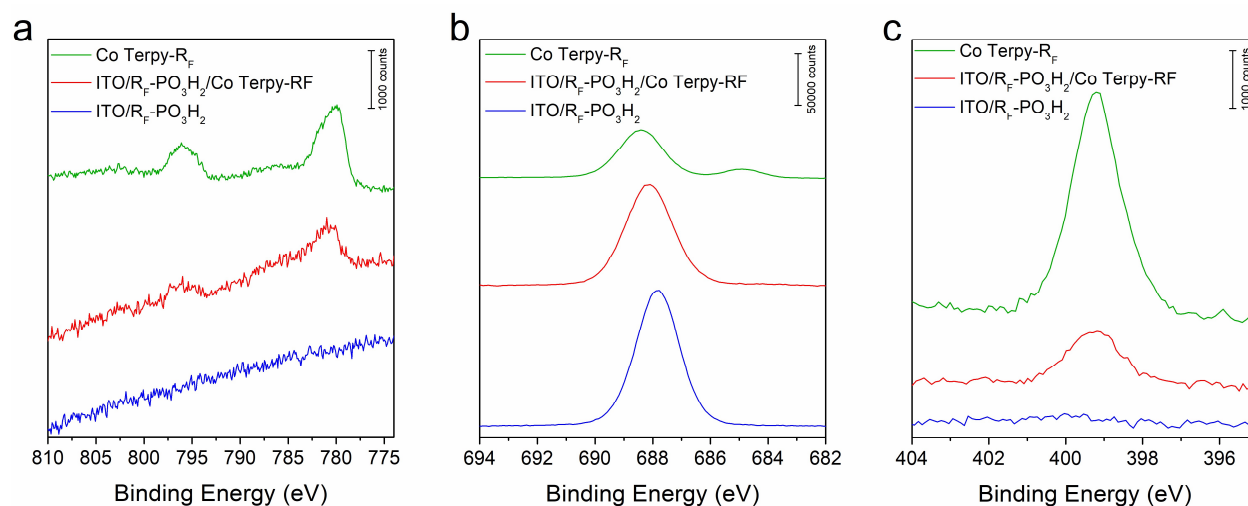
Figure S8. XPS spectra of the Co Terpy-R$_F$ adsorbed via hydrophobic interactions to an ITO surface modified with (1*H*,1*H*,2*H*,2*H*-heptadecafluorodec-1-yl)phosphonic acid. Spectra showing the Co 2p (a), F 1s (b) and N 1s (c) regions of (green) neat [Co(terpy-R$_F$)$_2$](BF$_4$)$_2$, (blue) ITO modified with a fluorous linker (blue) and [Co(terpy-R$_F$)$_2$](BF$_4$)$_2$ attached to fluorous ITO (red).
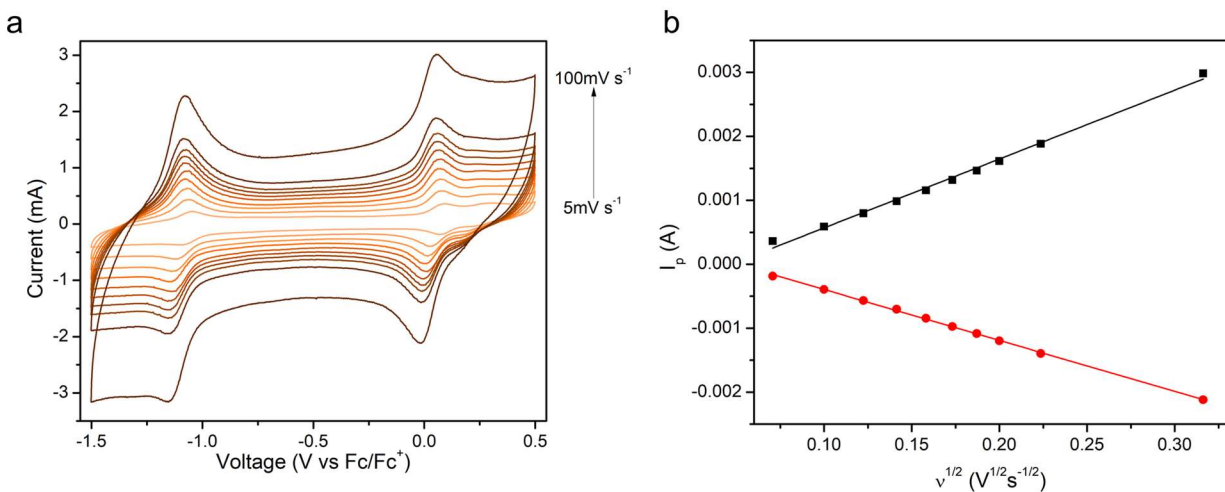
Figure S9. Cyclic voltammetry of a 1 mM acetonitrile solution of Co Terpy-R_F at various scan rates from 5 mVs^{-1} to 100 mVs^{-1} (a), $i_{p,a}$ and $i_{p,c}$ curves vs. the square root of the scan rate (b).
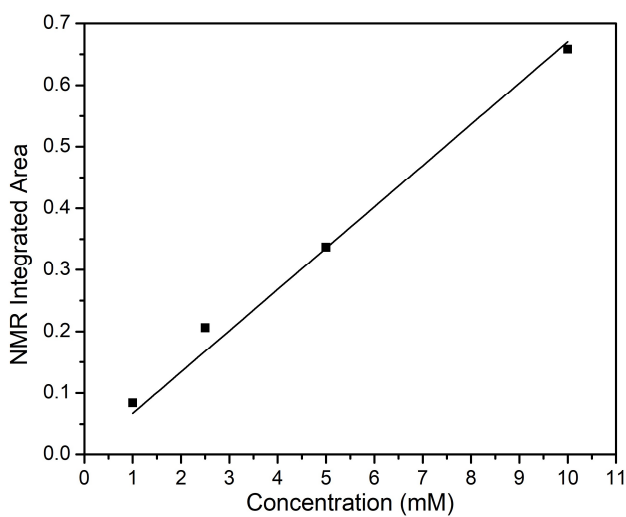
Figure S10. NMR calibration curve of formate. The relative peak area is plotted vs. that of the DMSO internal standard.
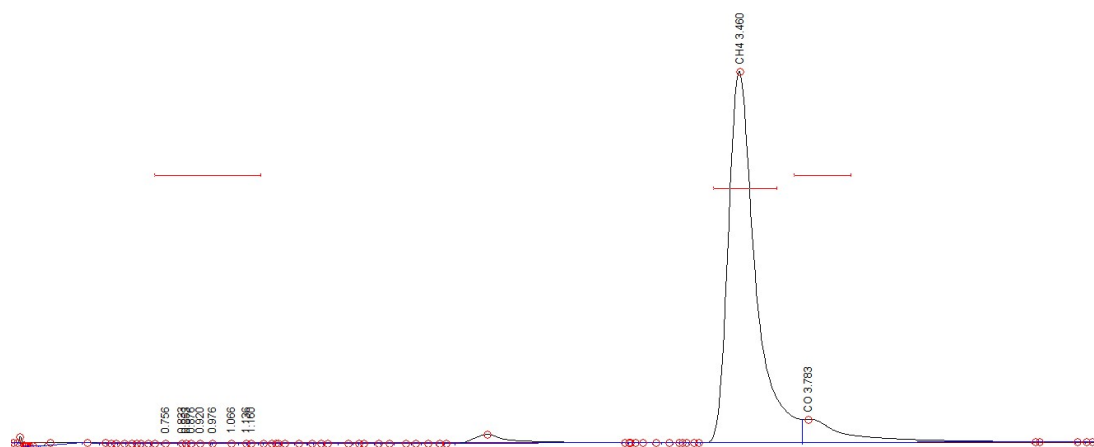
Figure S11. Gas chromatogram FID channel after 30 minutes of electrolysis at -1.89 V vs RHE showing CH_4 and CO peaks
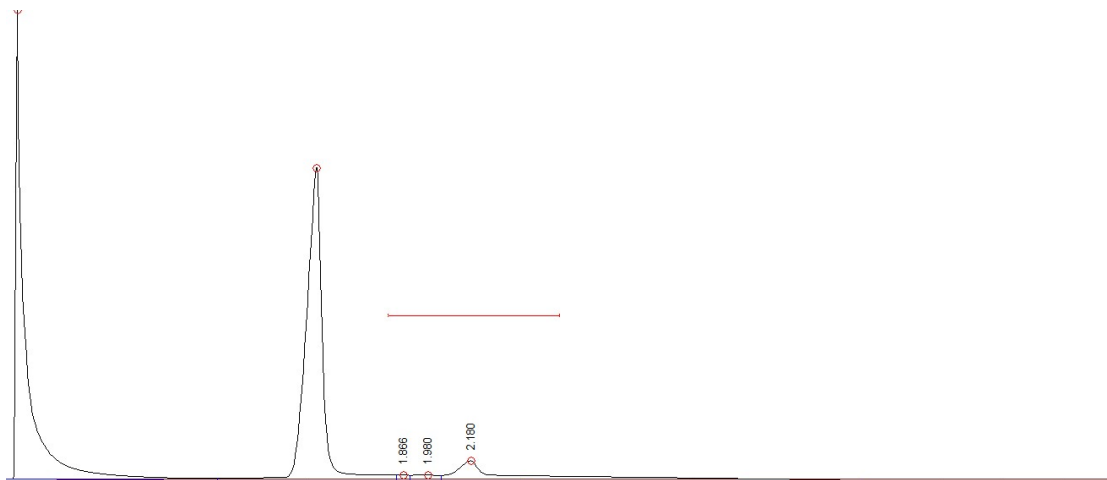
Figure S12. Gas chromatogram TCD channel after 30 minutes of electrolysis at -1.89 V vs RHE.
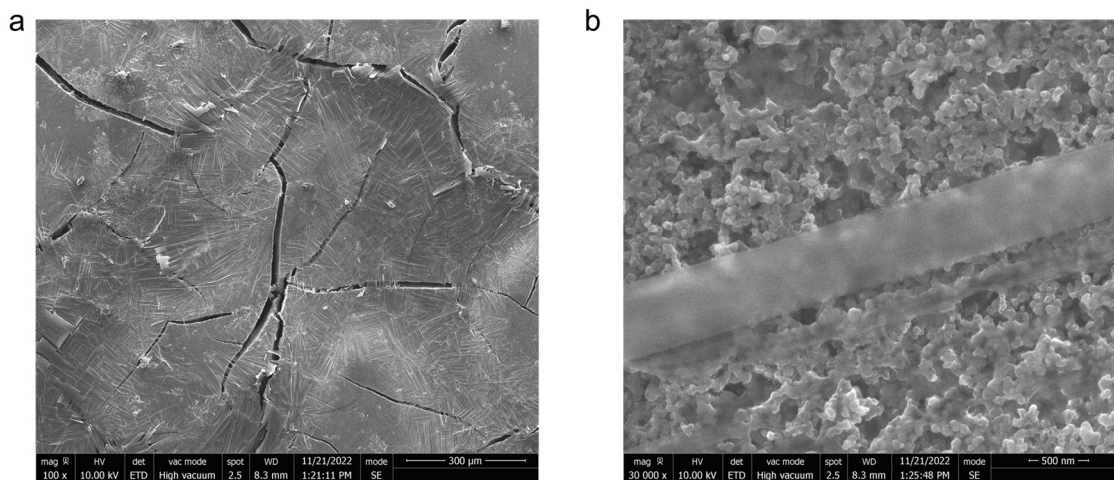
Figure S13. SEM images of Co Terpy-R_F drop cast onto a carbon cloth GDE at low (a) and high (b) magnifications.
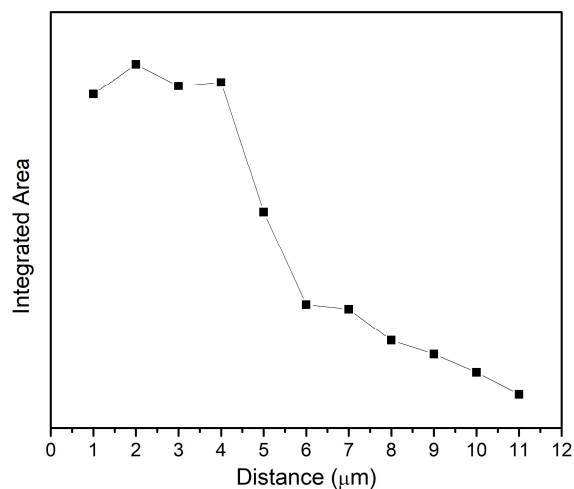
Figure S14. Raman mapping of a cross-section of Co Terpy-R_F on carbon cloth taken at 1 μm intervals. The integrated area of peak 1479 cm^{-1} is plotted against distance (depth).
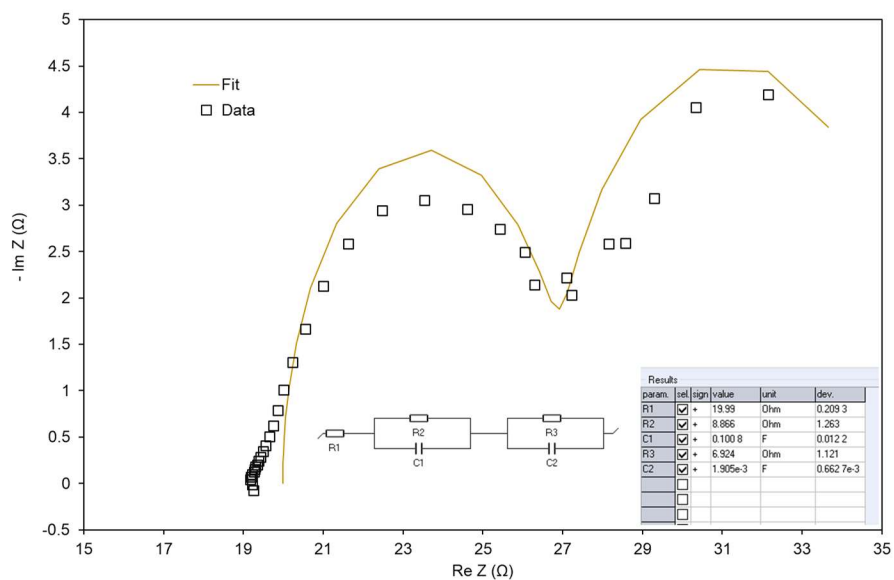
Figure S15. EIS analysis and fitting of Co Terpy-R_F film deposited on a GDE electrode at -0.58 V vs. RHE under CO_2 flow. Two semi-circles represent two resistances in series, attributed to charge transfer through the catalyst film and catalysis at active sites.
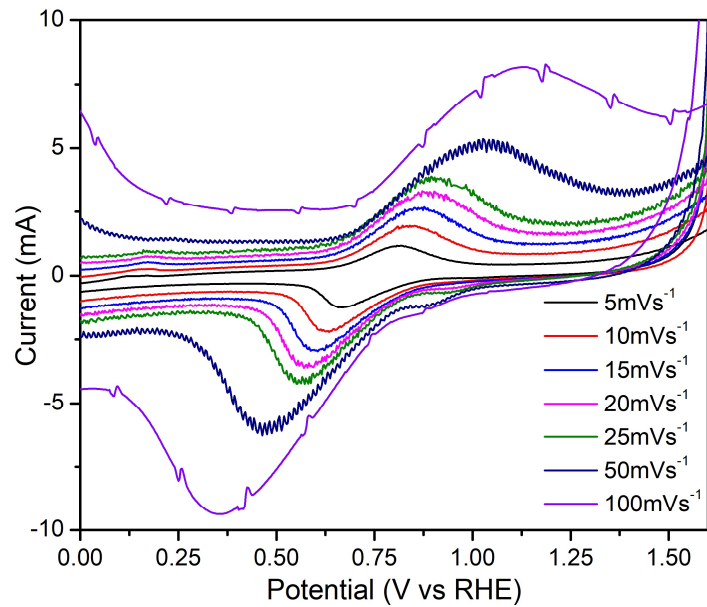
Figure S16. Cyclic voltammetry of Co Terpy-R_F on a GDE at various scan rates from 5 mVs^{-1} to 100 mVs^{-1}.
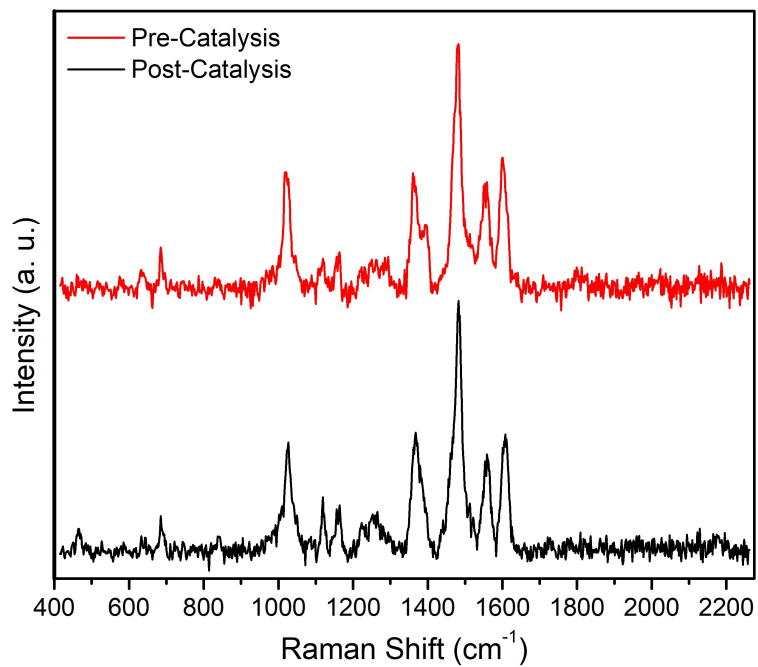
Figure S17. Raman spectrum of Co Terpy-R_F on C-cloth taken pre-catalysis and after 9 hours of electrolysis at -0.79 V vs. RHE.
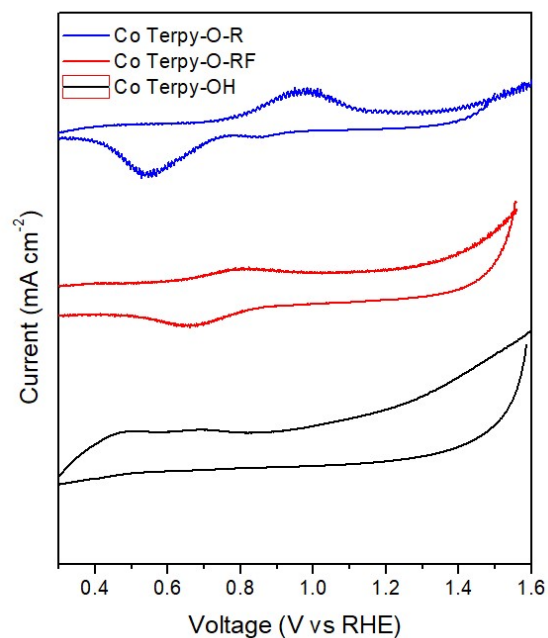
Figure S18. CVs of the Co Terpy analogs drop cast onto a GDE under N_2 in 0.5 M $KHCO_3$.
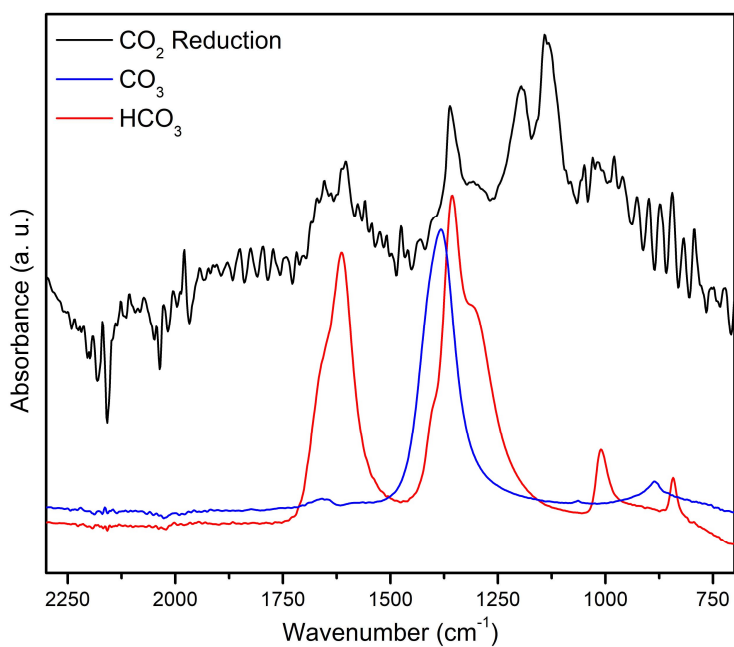

Figure S19. IR spectrum of $KHCO_3$ and K_2CO_3 dissolved in water overlaid with a typical spectrum during CO_2 reduction in 0.5M $KHCO_3$ at -0.79 V vs. RHE. Peaks around 1600 and 1300 cm^{-1} are attributed to HCO_3^- while peaks around 1000-1200 cm^{-1} stem from the carbon cloth electrode itself. The peak at 1640 cm^{-1}, however is attributed to a CO_2 reduction intermediate.
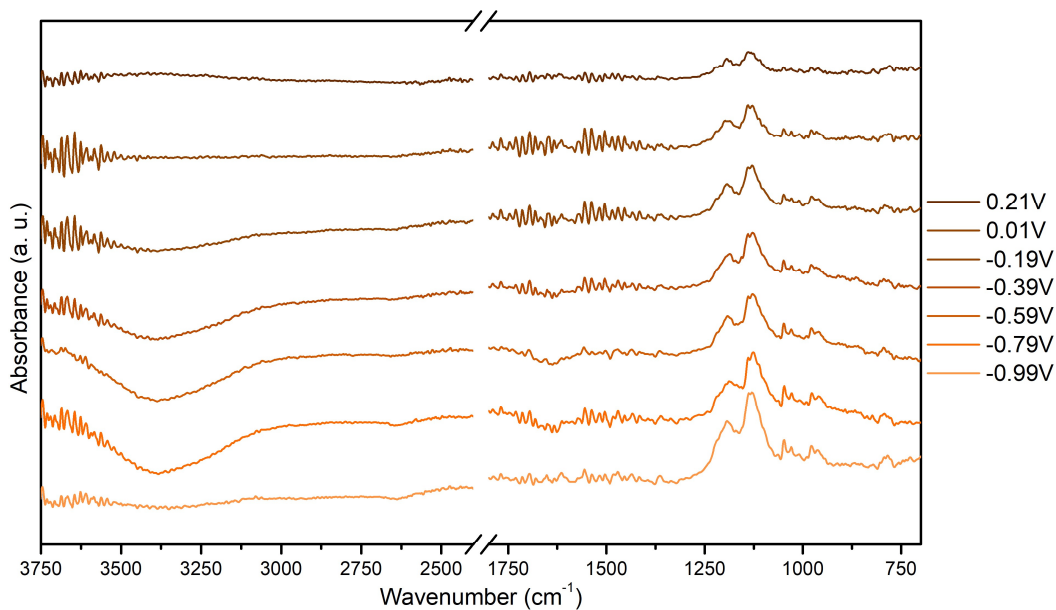
Figure S20. *in-situ* IR measurements under N_2, using the spectrum at open circuit as the background, spectra under select operating potentials were recorded (potentials give vs. RHE).
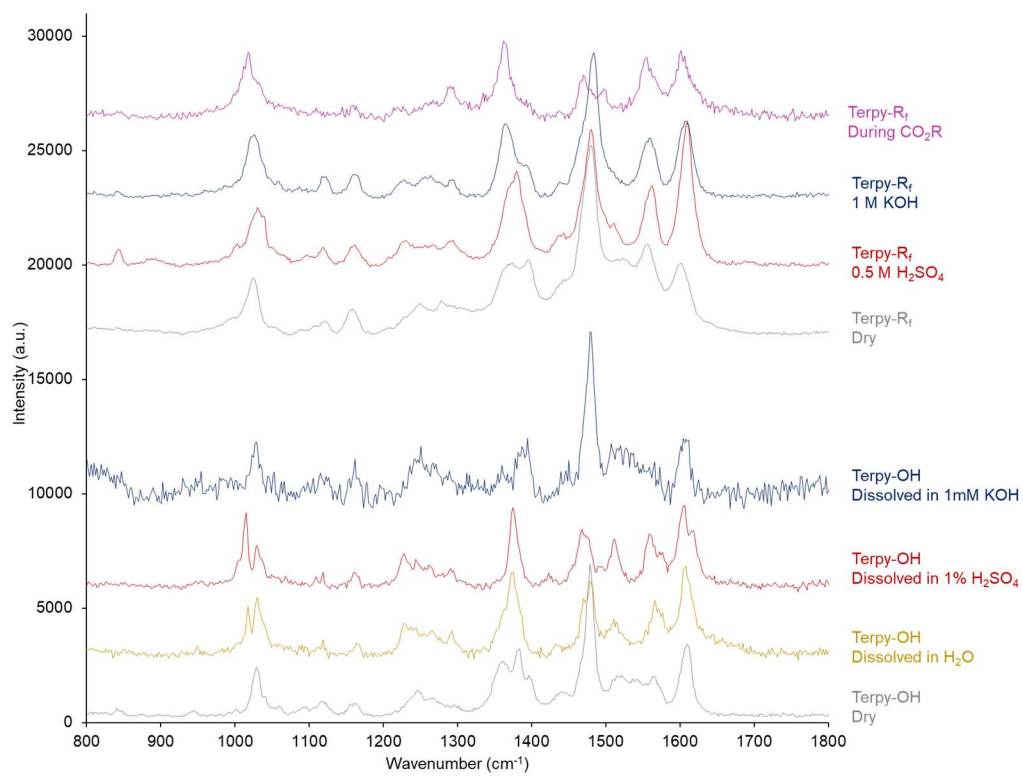
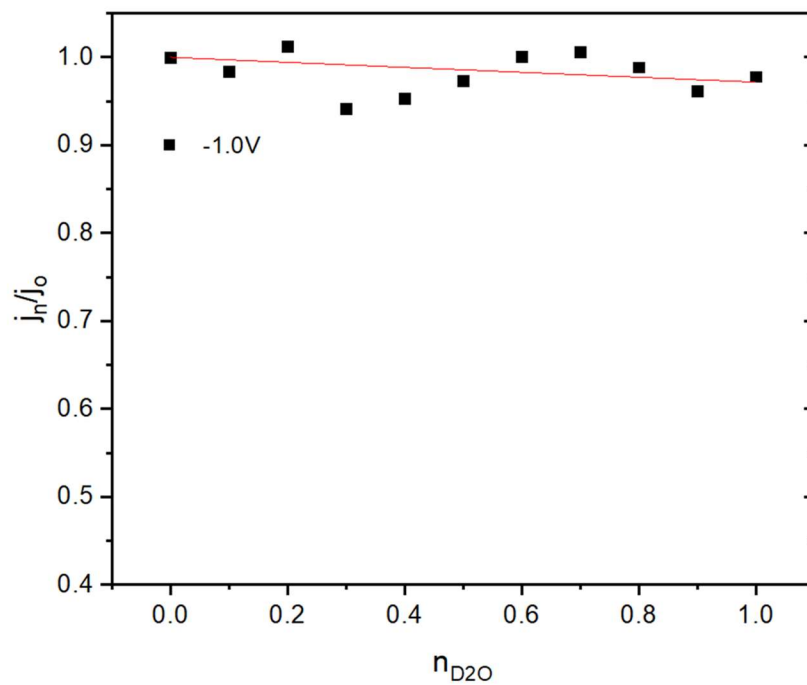**Figure S21.** Raman spectra of the Co Terpy catalysts under various conditions.

Figure S22. Proton inventory studies of the Co Terpy-R_F at -1.0V vs. Ag/AgCl just prior to the Co(II/I) redox potential. In this regime, the catalyst is not yet active and current only stems from the exposed areas of the carbon cloth electrode, where proton shuttling should not be in play. Indeed, only a linear fit is obtained with Z being close to 1.
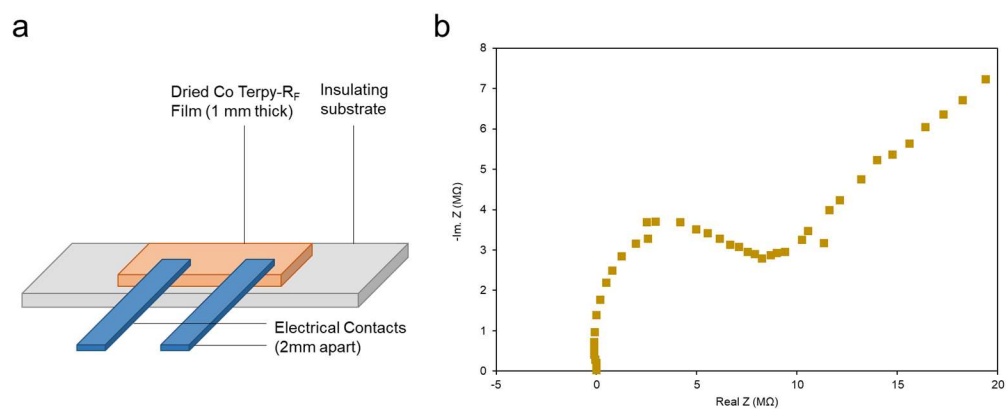
Figure S23. Simplified setup for proton conductivity measurements (a) and Nyquist impedance data (b) that give a conductance value of approx. 12 M ohms.
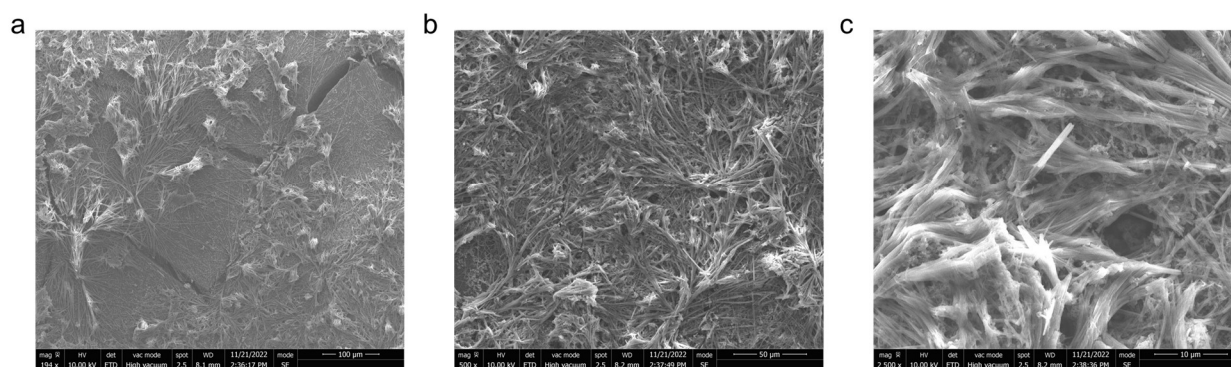

Figure S24. Co Terpy-R_F/F-CNT electrode at low (a), medium (b) and high (c) magnifications before electrolysis.
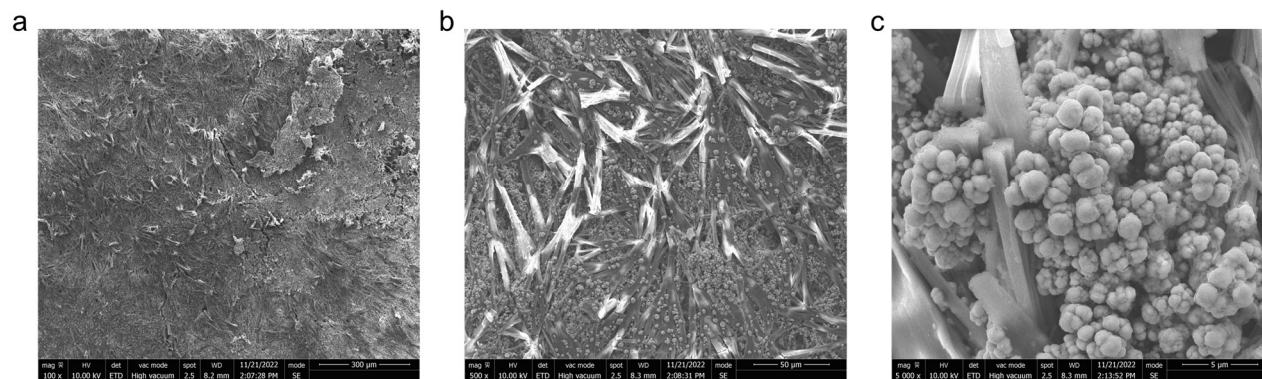
Figure S25. Co Terpy-R_F/F-CNT electrode at low (a), medium (b) and high (c) magnifications after 9 h electrolysis at –0.59 V vs. RHE.
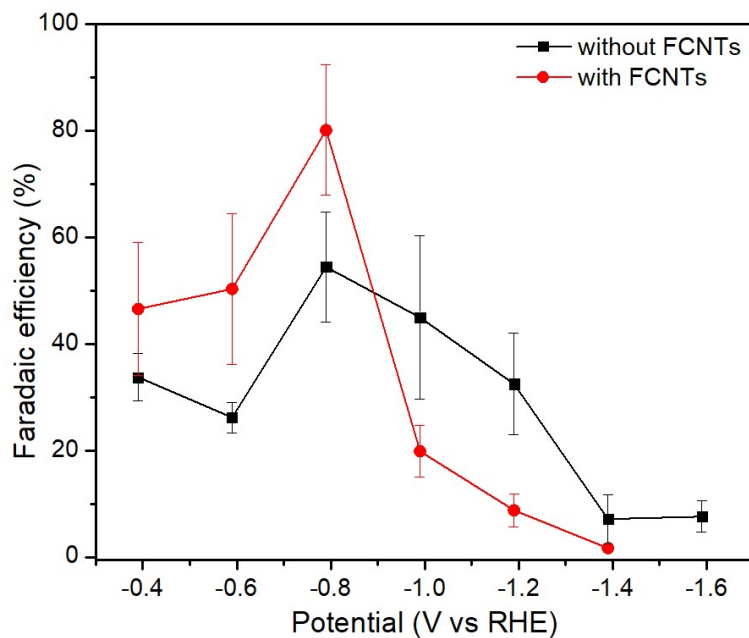
Figure S26. The Co Terpy-R$_F$/F-CNT system shows an earlier degradation onset, possibly due to better wiring to the electrode, and thus an earlier drop in the CH$_4$ FE.
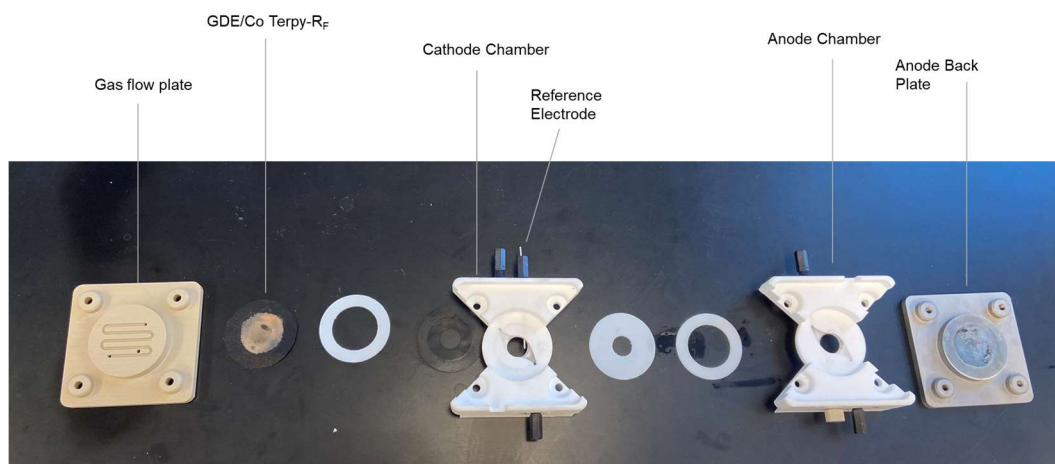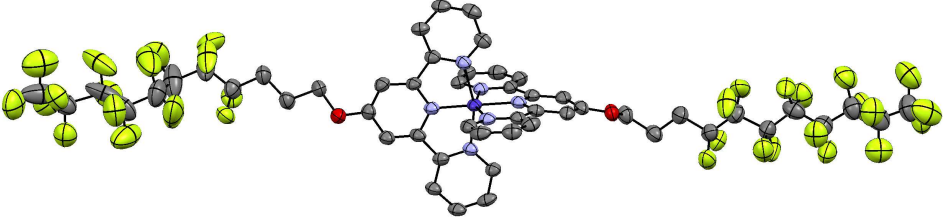

Figure S27. Disassembled flow cell containing Co Terpy-R$_F$ GDE electrodes from Sphere Energy SAS used to monitor CH$_4$ production over extended time frames.

Table S1. Experimental X-ray diffraction parameters and crystal data for [Co(terpy-R$_F$)$_2$](BF$_4$)$_2$.

Chemical formula	C$_{52}$H$_{32}$CoB$_2$F$_{42}$N$_6$O$_2$	F(000)	1650
Formula weight	1651.34	Crystal size	0.09 × 0.05 × 0.03 mm^3
Temperature	100(2) K	Absorption coefficient	3.872 mm^{-1}
Wavelength	1.54178 Å	Index ranges	-8<=h<=10 -23<=k<=23 -24<=l<=24
Crystal system	triclinic	Reflections collected	46546
Space group	*P*-1	Independent reflections	11168
Lattice constants	a = 8.9227(2) Å	Completeness to 67.679°	99.6 %
	b = 19.1606(5) Å	Absorption correction	multi-scan
	c = 20.2888(8) Å	Max. and min. transmission	0.5210 and 0.3976
	α = 118.1630(10)°	Refinement method	Full-matrix least-squares on F^2
	β = 92.264(2)°	Data / restraints / parameters	11168 / 0 / 955
	γ = 91.957(2)°		
Volume	3050.12(16) Å^3	Final R indices [I>2sigma(I)]	R$_1$ = 0.1472 wR$_2$ = 0.3895

Z	2	Largest diff. peak and hole	1.854 and -0.914 e.Å^{-3}
Density (calculated)	1.816 Mg/m^3	**Goodness-of-fit on F^2**	1.590

Table S2. Select Molecular catalysts integrated with a GDE electrode

Catalyst	Electrolyte	Products	FE (%)	j (mA cm^{-2})	REF
[Ag(I)(4-OMe-BIAN)$_2$]BF$_4$	1M KHCO$_3$	CO	51	50	*Catalysts,* 2022, **12**, 545.
[Ni(Cyc)]$^{2+}$	MEA configuration	CO	63	16	*J. Am. Chem. Soc.,* 2022, **144**, 7551–7556
[Ni(CycCOOH)]$^{2+}$	MEA configuration	CO	48	11	*J. Am. Chem. Soc.,* 2022, **144**, 7551–7556
CoPc	MEA configuration	CO	95	175	*Science,* 2019, **365**, 367–369.
CoPc2@carbon black	1M KOH	CO	96	165	*Nat. Commun.,* 2019, **10**, 3602.

Table S3. Cobalt terpyridine catalysts in homogeneous systems

Catalyst	Electrolyte	Products	FE (%)	j (mA cm^{-2})	REF
1: PhCl substituted	DMF/H$_2$O (95 : 5), TBAPF$_6$ 0.1 M	CO	31	9.3	*Chem. Sci.,* 2015, **6**, 2522–2531.
2: PhMe substituted	DMF/H$_2$O (95 : 5), TBAPF$_6$ 0.1 M	CO	12	3.6	*Chem. Sci.,* 2015, **6**, 2522–2531.

3: unsubstituted	DMF/H_2O (95 : 5), TBAPF$_6$ 0.1 M	CO	11	3.3	*Chem. Sci.*, 2015, **6**, 2522–2531.
4: OMe substituted	DMF/H_2O (95 : 5), TBAPF$_6$ 0.1 M	CO	4	1.2	*Chem. Sci.*, 2015, **6**, 2522–2531.
5: ^{t}Bu substituted	DMF/H_2O (95 : 5), TBAPF$_6$ 0.1 M	CO	37	11.1	*Chem. Sci.*, 2015, **6**, 2522–2531.

Table S4: Our Results

Catalyst	Electrolyte	Products	FE (%)	j (mA cm^{-2})	REF
$[Co(tpy\text{-}O\text{-}R_F)_2]^{2+}$	MeCN/H$_2$O (95 : 5), TBAPF$_6$ 50mM	CO	8.4	0.012	This work
$[Co(tpy\text{-}O\text{-}R_F)_2]^{2+}$ (GDE)	0.5M KHCO$_3$	CH$_4$	54	4.50	This work
$[Co(tpy\text{-}O\text{-}R_F)_2]^{2+}$ with F-CNTs (GDE)	0.5M KHCO$_3$	CH$_4$	80	10.69	This work
$[Co(tpy\text{-}OH)_2]^{2+}$	0.5M KHCO$_3$	CO	0.07	0.007	This work
$[Co(tpy\text{-}O\text{-}(CH_2)_9CH_3)_2]^{2+}$	0.5M KHCO$_3$	CH$_4$	10.6	1.08	This work